PCCP

ROYAL SOCIETY OF CHEMISTRY

PAPER

View Article Online
View Journal | View Issue

Cite this: *Phys. Chem. Chem. Phys.*, 2024, **26**, 12306

Gas-phase electronic spectra of $HC_{2n+1}H^+$ (n = 2–6) chains†

Samuel J. P. Marlton, Chang Liu, Patrick Watkins and Evan J. Bieske *

Highly unsaturated carbon chains are generated in combustion processes and electrical discharges, and are confirmed constituents of the interstellar medium. In hydrogen-rich environments smaller carbon clusters tend to exist as linear chains, capped on each end by hydrogen atoms. Although the $HC_{2n}H^+$ polyacetylene chains have been extensively characterized spectroscopically, the corresponding odd $HC_{2n+1}H^+$ chains have received far less attention. Here we use two-colour resonance enhanced photodissociation spectroscopy to measure electronic spectra for $HC_{2n+1}H^+$ (n = 2–6) chains contained in a cryogenically cooled quadrupole ion trap. The $HC_{2n+1}H^+$ chains are formed either top-down by ionizing and fragmenting pyrene molecules using pulsed 266 nm radiation, or bottom-up by reacting cyclic carbon cluster cations with acetylene. Ion mobility measurements confirm that the $HC_{2n+1}H^+$ species are linear, consistent with predictions from electronic structure calculations. The $HC_{2n+1}H^+$ electronic spectra exhibit three band systems in the visible/near infrared spectral range, which each shifts progressively to longer wavelength by ≈90 nm with the addition of each additional C═C subunit. The strongest visible $HC_{11}H^+$ band has a wavelength (λ = 545.1 nm) and width (1.5 nm) that match the strong λ 5450 diffuse interstellar band (DIB). However, other weaker $HC_{11}H^+$ bands do not correspond to catalogued DIBs, casting doubt on the role of $HC_{11}H^+$ as a carrier for the λ 5450 DIB. There are no identifiable correspondences between catalogued DIBs and bands for the other $HC_{2n+1}H^+$ chains, allowing upper limits to be established for their column densities in diffuse interstellar clouds.

Received 12th February 2024,
Accepted 8th April 2024

DOI: 10.1039/d4cp00625a

rsc.li/pccp

1 Introduction

Polyynes and highly unsaturated carbon chains (C_nH_m, $C_nH_m^+$, $C_nH_m^-$, with m = 1, 2) are confirmed constituents of the interstellar medium (ISM), particularly in molecular clouds such as the starless core TMC-1, where they have been detected through their microwave and infrared transitions.[1–5] Although carbon chain molecules are prevalent in molecular clouds, they are typically less abundant in hot molecular cores, translucent clouds, and diffuse clouds.[6] Highly unsaturated carbon chains were also proposed as potential carriers of diffuse interstellar bands (DIBs), discrete spectral features occurring across the visible and near infrared spectral ranges that are presumed to arise from the absorptions of molecules in diffuse molecular clouds.[7–9] Although more than 500 DIBs have been identified, the only known carrier is the C_{60}^+ fullerene, which is associated with five DIBs.[10,11]

The widespread importance of carbon chains and the ease with which they can be generated has motivated several laboratory investigations of their infrared and electronic transitions.[6,12–17] Electronic spectra for bare carbon chains have been recorded for neutral,[18–21] cation,[22–24] and anion species.[25–27] For hydrogenated species, electronic spectra have been measured for neutral C_nH chains up to n = 16,[27] C_nH^+ chains up to n = 17,[28] and C_nH^- chains up to n = 24.[14,29] Neutral C_nH (n = 2–9) chains have also been characterized through photoelectron spectra of anion C_nH^- chains.[30,31] Electronic spectra have been measured for polyacetylene cations as large as $HC_{14}H^+$.[32,33] In work related to the current study, the $A^3\Sigma_u^- \leftarrow X^3\Sigma_g^-$ electronic band systems of neutral $HC_{2n+1}H$ (n = 3–6) chains have been measured using cavity ring down spectroscopy, confirming that these species have linear, centrosymmetric structures.[34] The visible electronic transitions of neutral $HC_{2n+1}H$ (n = 3–6) chains have also been studied using resonance enhanced two-colour photoionization spectroscopy.[35]

Here we examine the $HC_{2n+1}H^+$ chains through their electronic absorptions in a cryogenically cooled ion trap, extending our earlier spectroscopic studies of bare and hydrogenated carbon clusters, including C_n^+ cyclocarbons,[36,37] and singly hydrogenated carbon chains and rings $C_{2n+1}H^+$.[28] As they lack a permanent dipole moment, the $HC_{2n+1}H^+$ chains cannot easily be detected using microwave spectroscopy so their investigation in the ISM necessarily relies on either their electronic

School of Chemistry, University of Melbourne, Parkville 3010, Australia.
E-mail: evanjb@unimelb.edu.au

† Electronic supplementary information (ESI) available. See DOI: https://doi.org/10.1039/d4cp00625a

or infrared transitions. The only previously reported electronic spectra for the $HC_{2n+1}H^+$ chains (n = 2–7) are for ions embedded in a neon matrix.[19,22,38] These matrix spectra exhibited several different band systems, that were interpreted with the aid of multireference electronic structure calculations.[39,40] Although the Ne matrix spectra are useful for identifying relevant transitions and assessing their relative intensities, the lines are broadened and shifted in wavelength due to ion-matrix interactions. Potentially, there are also contributions to the spectra from neutral molecules in the matrix. The higher resolution gas-phase spectra reported here provide the first opportunity for comparisons with astronomical data and for gauging the presence of $HC_{2n+1}H^+$ chains in the ISM.

Although $HC_{2n+1}H^+$ chains are yet to be detected in space, they may be produced in different regions through ion–molecule reactions. For example, flow tube studies show that $C_5H_2^+$ is generated efficiently from the reaction of C_3H^+ and C_4H_2.[41] This and similar reactions may occur in protoplanetary disks in which diacetylene has recently been detected.[42] Other formation mechanisms could involve protonation of neutral $C_{2n+1}H$ molecules by H_3^+ or HCO^+. Laboratory studies show that $HC_{2n+1}H^+$ ions are also produced through reactions of carbon cluster cations with acetylene, such as:[43]

$$C_n^+ + C_2H_2 \rightarrow C_{n-1}H_2^+ + C_3$$

$$C_n^+ + C_2H_2 \rightarrow C_{n+2}H_2^+$$

The first reaction occurs for C_4^+, C_6^+ and C_8^+, which are presumably mainly linear molecules, and is favoured by the stability of the C_3 co-fragment. The second reaction occurs over a size range for which the carbon cluster population consists of linear and cyclic isomers (C_7^+, C_8^+, C_9^+) or only cyclic isomers (C_{10}^+, C_{11}^+, C_{12}^+ C_{13}^+, C_{14}^+).[43] The reactivity of small cyclo-carbon cations with acetylene stands in contrast to their unreactivity with many other molecules, including H_2, D_2,[44] O_2,[44] CH_4,[44] N_2O,[45] and HCN.[46] Hydrogenated carbon chains might also be formed top-down through photodissociation of PAHs or other large hydrocarbon molecules.[47–49] In the current study, we mimic this route by generating $HC_{2n+1}H^+$ chains by ionizing and dissociating pyrene molecules using pulsed 266 nm radiation.

2 Experimental methods

The experimental setup has been described previously.[28,36,50] The apparatus, shown in Fig. 1, consists of several linked stages that include an ion source, an ion mobility drift tube, a hexapole ion guide/pretrap where the ions were accumulated, a quadrupole mass filter, an octopole ion guide, a cryogenically cooled quadrupole ion trap (QIT), and a time-of-flight mass spectrometer. The $HC_{2n+1}H^+$ ions were generated in two ways, which are illustrated in Fig. 1 (Schemes 1 and 2). First, as shown in Fig. 1 (Scheme 1), the $HC_{2n+1}H^+$ ions were produced by exposing vapour emanating from a solid pyrene sample (vapor pressure $P \approx 5\times 10^{-6}$ torr at 300 K) with the fourth harmonic of a pulsed Nd:YAG laser (λ = 266 nm, 50 μJ per pulse, 100 Hz). The ions passed through a drift tube ion mobility spectrometer (IMS) containing He buffer gas at ≈3 torr, propelled by a ≈10 V cm^{-1} electric field. The drift tube IMS served to separate the ions spatially and temporally according to their collision cross sections with He buffer gas. When required, an electrostatic Bradbury–Nielsen ion gate positioned at the end of the drift region was used to select ions with a particular range of collision cross sections. Following the drift region the ion packet was compressed radially by an RF ion funnel and passed through a 1 mm orifice in a differential wall and then into an RF hexapole ion guide. Ions were accumulated in the hexapole for 50 shots of the ablation laser, then released to travel through a quadrupole mass filter (QMF). Ions then passed through an octupole ion guide and into a three-dimensional quadrupole ion trap (QIT) connected to a cryo-head, where they were cooled to ≈10 K through collisions with He gas introduced through a pulsed nozzle operating at 2 Hz.

Electronic action spectra of $HC_{2n+1}H^+$ ions were recorded using two-colour resonance enhanced photodissociation (REPD) by monitoring $C_{2n+1}H^+$ and C_{2n+1}^+ photofragments (corresponding to loss of H, 2H, or H_2), and also for $HC_{13}H^+$ the C_{11}^+ photofragment (loss of HCCH). After 400 ms in the QIT, ions were exposed to a single pulse of light from a tunable optical parametric oscillator (OPO, EKSPLA NT342B, 6 ns pulse, bandwidth ≈4 cm^{-1}) followed 10 ns later by a pulse of fixed-wavelength light from a second OPO (EKSPLA NT340, 6 ns pulse width, bandwidth ≈4 cm^{-1}). The spectra in the visible region were normalised with respect to the laser power at each wavelength. The wavelength of the OPO output was measured using a wavemeter (Ångstrom High Finesse). The wavelength of the second OPO output was chosen to maximise the resonant two-colour photofragment signal, while minimising the signal produced by the second OPO alone, and was 440 nm for HC_5H^+, 500 nm for HC_7H^+, 550 nm for HC_9H^+, 450 nm for $HC_{11}H^+$, and 235 nm for $HC_{13}H^+$.

The $HC_{2n+1}H^+$ chains were also synthesised by reacting carbon cluster cations with acetylene as shown in Fig. 1 (Scheme 2). The carbon cluster cations were generated by laser ablation of a graphite disk with the second-harmonic of the Nd:YAG ablation laser (λ = 532 nm) and passed through the IMS stage. Specific carbon cluster isomers were selected by their arrival time (t_a) using the Bradbury–Nielson ion gate. Ion mobility arrival time distributions were measured by scanning the delay between firing the ablation laser and opening the Bradbury–Nielsen ion gate. The mobility-selected ions then passed into the hexapole ion guide where they were stored for up to 500 ms. The hexapole region contained a 2% acetylene in argon gas mixture ($P \approx 2\times 10^{-4}$ torr, acetylene number density ≈10^{11} cm^{-3}). Ions exiting the hexapole passed through the QMF and octupole ion guide and into the QIT where they were probed spectroscopically as described above for Scheme 1.

It should be emphasized that the $HC_{2n+1}H^+$ molecules do not dissociate directly following excitation to the lower electronic states (Ã, B̃ and C̃ states), but require absorption of an additional photon or photons from the second laser. Without the second laser pulse, there was essentially no photodissociation.

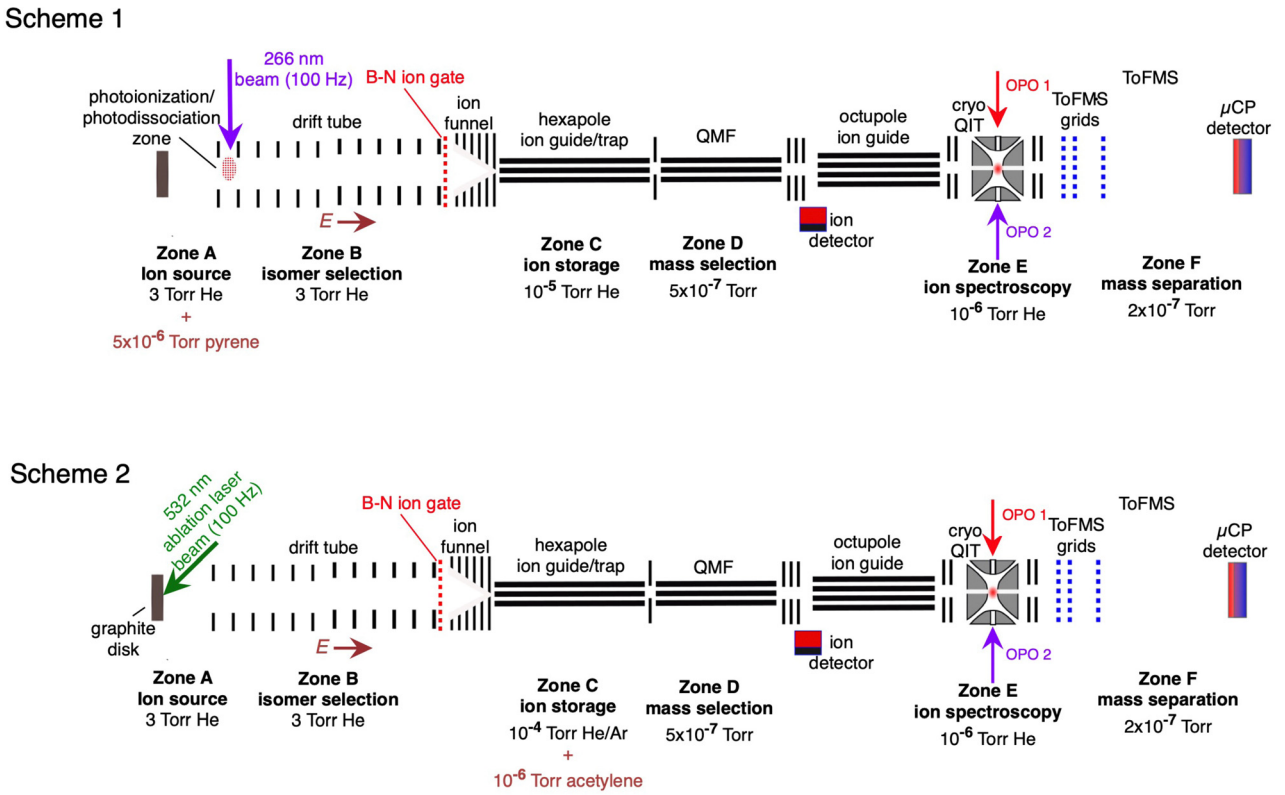

Fig. 1 IMMS-cryotrap instrument for obtaining electronic spectra of $HC_{2n+1}H^+$ chains. $HC_{2n+1}H^+$ chains were formed in two different ways. Scheme 1: $HC_{2n+1}H^+$ chains were produced by exposing pyrene vapour ($P \approx 5 \times 10^{-6}$ torr) to pulsed 266 nm radiation, which induced ionization and fragmentation. Following formation, the ions passed through an ion mobility drift tube, which served to separate different isomers. At the end of the drift tube there is a Bradbury–Nielsen (B–N) ion gate that could be used to select a particular isomer. Ions were then accumulated in a hexapole ion guide. Following ejection from the hexapole, the ions passed through a quadrupole mass filter (QMF), and an octupole ion guide, before being trapped in a cryogenically cooled quadrupole ion trap (QIT). In the QIT the ions were exposed to tunable light from an OPO overlapped (spatially and temporally) with a fixed wavelength beam from a second OPO. Resulting photofragments were separated and detected using a time-of-flight mass spectrometer. Scheme 2: $HC_{2n+1}H^+$ chains were produced by reacting carbon chains (C_n^+), formed through laser ablation of a graphite disk, with acetylene gas at a partial pressure of $\approx 2 \times 10^{-6}$ torr in the hexapole ion guide for ≈ 0.5 s. If required, the reactant C_n^+ ions could be mobility-selected in the drift tube using the B–N ion gate. Following their creation in the hexapole, the $HC_{2n+1}H^+$ ions were mass-selected and spectroscopically probed in the QIT as described for Scheme 1.

This is consistent with bond dissociation energies (D_0) calculated for $C_5H_2^+$ at the CCSD(T)/cc-pVTZ level of theory using optimized geometries found at the TPSSh/def2-TZVP level of theory. The calculated dissociation energies are:

(a) $C_5H^+(^1\Sigma^+) + H(^2S_{1/2})$ 4.28 eV
(b) l-$C_5^+(^2\Sigma_u^+) + H_2(^1\Sigma_g^+)$ 6.28 eV
(c) c-$C_3^+(^2B_2) + C_2H_2$ $(^1\Sigma_g^+)$ 6.65 eV
(d) l-$C_3^+(^2\Sigma_u^+) + C_2H_2$ $(^1\Sigma_g^+)$ 6.99 eV

Therefore, the lowest energy dissociation channel (H-loss) should have a single-photon onset at around 290 nm, at a shorter wavelength than investigated in the current study. A similar situation should prevail for the larger $HC_{2n+1}H^+$ chains for which the Ã, B̃ and C̃ states progressively shift to lower energies. The photodissociation yields did not depend on the delay between the first and second laser pulses (out to 10 μs) indicating that the molecules undergo rapid internal conversion following excitation to the Ã, B̃ and C̃ states and that the second photon delivers sufficient additional energy to take the vibrationally excited ions above the dissociation threshold.

3 Quantum chemical calculations

The $HC_{2n+1}H^+$ chains were investigated computationally using the CAM-B3LYP density functional theory method[51] including empirical dispersion (D3BJ)[52] and the triple zeta def2-TZVP basis set.[53] These geometries were employed for electronic structure calculations using the complete active space self consistent field (CASSCF)[54] method with the def2-TZVP basis set taking spin–orbit coupling into account as implemented in the ORCA/5.0.2 program package.[55] CASSCF calculations were undertaken for HC_5H^+, HC_7H^+, and HC_9H^+ using the active spaces recommended in ref. 39 with averaging over eight doublet and eight quartet states. We tested this approach by calculating the spin–orbit coupling constants of C_7^- and HC_4H^+. For C_7^-, the active space was comprised of nine electrons in two σ and eight π orbitals, which yielded spin–orbit constants $A''_{SO} = 27\ cm^{-1}$ (experimental value 27.4 cm^{-1}) and $A'_{SO} = 3\ cm^{-1}$ (experimental value 0.6 cm^{-1}).[56] For HC_4H^+, the active space was comprised of seven electrons in eight π

orbitals, which yielded spin–orbit constants $A''_{SO} = -31$ cm^{-1} (experimental value -31.1 cm^{-1}) and $A'_{SO} = -28$ cm^{-1} (experimental value -30 cm^{-1}).[33,57] The equilibrium geometry and ground state rotational constant of HC_5H^+ were calculated using the CCSD(T) method[58] with the TZVP basis set[59] in the ORCA program package.[55]

4 Results and discussion

4.1 Electronic structure of $HC_{2n+1}H^+$ chains

Before reporting and discussing the electronic spectra it is worth briefly reviewing the electronic states and transitions of the $HC_{2n+1}H^+$ linear molecules. As described previously,[38–40,60] the $\tilde{X}^2\Pi_{u/g}$ ground state of the linear $HC_{2n+1}H^+$ molecules is described by the $\ldots(n/2)\pi_u^4\,(n/2)\pi_g^4\,(n/2+1)\pi_u^1$ electronic configuration for n even, and $\ldots((n-1)/2)\pi_g^4\,((n+1)/2)\pi_u^4\,((n+1)/2)\pi_g^1$ configuration for n odd. These configurations give rise to $\tilde{X}^2\Pi_u$ and $\tilde{X}^2\Pi_g$ ground states for even and odd n, respectively.

There are three excited electronic states that are relevant for transitions in the 200–2000 nm range – the $1^2\Pi_{g/u}$, $2^2\Pi_{g/u}$ and $3^2\Pi_{g/u}$ states.[39] As explained in ref. 39, for $HC_{2n+1}H^+$ chains with n even, the $1\Pi_g$ and $2\Pi_g$ states have predominantly $\ldots(n/2)\pi_u^4\,(n/2)\pi_g^3\,(n/2+1)\pi_u^2$ configurations, whereas the $3\Pi_g$ state is an admixture of $\ldots(n/2)\pi_u^4\,(n/2)\pi_g^3\,(n/2+1)\pi_u^2$ and $\ldots(n/2)\pi_u^4\,(n/2)\pi_g^3\,(n/2+1)\pi_u^0\,(n/2+1)\pi_g^1$ configurations. For $HC_{2n+1}H^+$ chains with n odd, the $1^2\Pi_u$ and $2^2\Pi_u$ states have predominantly $\ldots((n-1)/2)\pi_g^4\,((n+1)/2)\pi_u^3\,((n+1)/2)\pi_g^2$ configurations, whereas the $3^2\Pi_u$ state is an admixture of $\ldots((n-1)/2)\pi_g^4\,((n+1)/2)\pi_u^3\,((n+1)/2)\pi_g^2$ and $\ldots((n-1)/2)\pi_g^4\,((n+1)/2)\pi_u^4\,((n+1)/2)\pi_g^0\,((n+3)/2)\pi_u^1$ configurations. In other words, the $\tilde{A}$ and $\tilde{B}$ states, are best described as SOMO ← SOMO−1 excitations, whereas SOMO ← SOMO−1 and LUMO ← SOMO excitations are important for the C state. The $1^2\Pi_{g/u} \leftarrow X^2\Pi_{u/g}$ and $2^2\Pi_{g/u} \leftarrow X^2\Pi_{u/g}$ transitions are predicted to be relatively weak compared to the $3^2\Pi_{g/u} \leftarrow X^2\Pi_{u/g}$ transition.[39] There is also an adjacent $^2\Phi_{g/u}$ state that is not optically coupled to the ground state. However, transitions to this state potentially gain intensity through vibronic coupling with the excited $\Pi_{g/u}$ states.[38] Previously Fulara *et al.* labelled the three lowest excited $\Pi_{u/g}$ states as $\tilde{A}^2\Pi_{u/g}$, $\tilde{B}^2\Pi_{u/g}$ and $\tilde{C}^2\Pi_{u/g}$ states,[38] a convention we retain in this paper.

4.2 Electronic spectra

The REPD spectra of $HC_{2n+1}H^+$ molecules (n = 2–6) are presented in Fig. 2. Wavelengths (λ_{air}), widths and assignments for

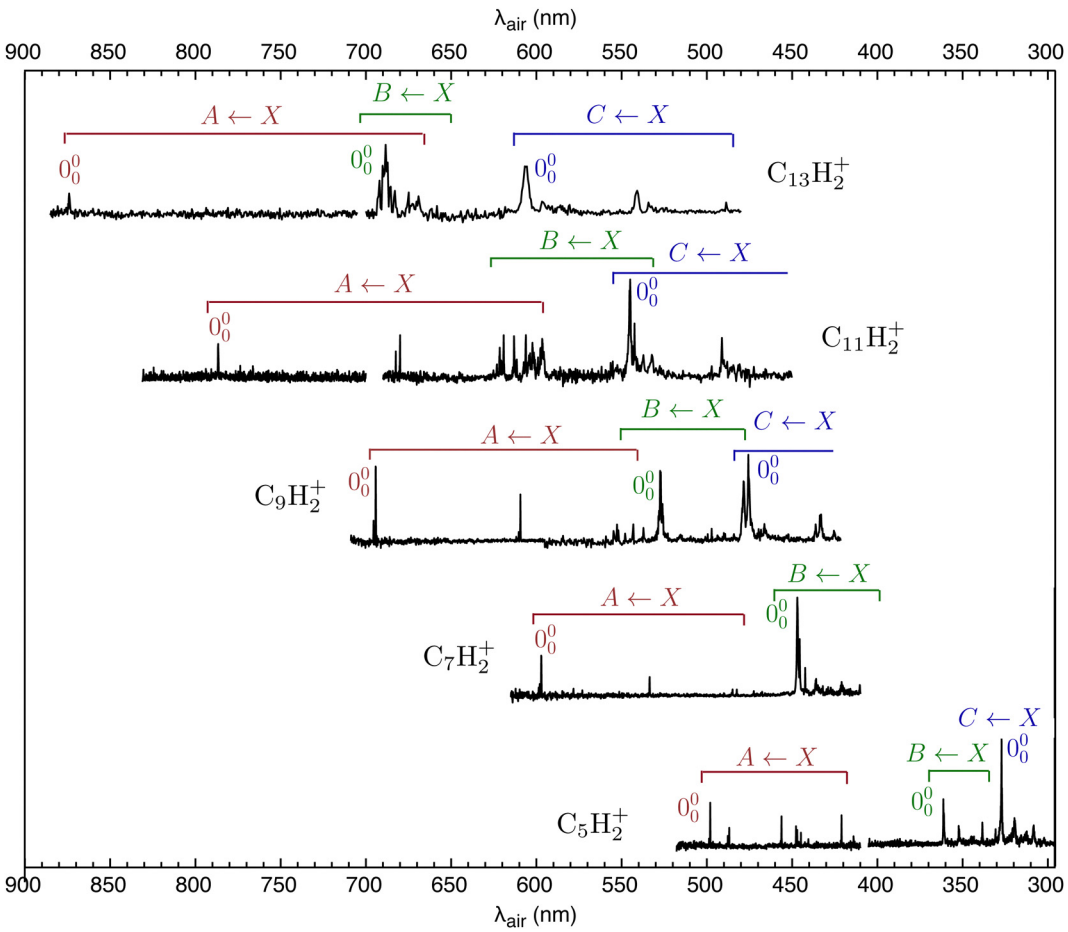

Fig. 2 Two-colour REPD spectra of $HC_{2n+1}H^+$ chains recorded by monitoring $C_{2n+1}H^+$ and C_{2n+1}^+ photofragments. Indicated are the origin bands and extent of the $\tilde{A} \leftarrow \tilde{X}$ (red), $\tilde{B} \leftarrow \tilde{X}$ (green) and $\tilde{C} \leftarrow \tilde{X}$ (blue) band systems. Gaps in the spectra near 710 nm and 410 nm correspond to drops in the OPO output power due to crystal changes.

the bands are given in Tables S2 and S3 in the ESI.† The $HC_{2n+1}H^+$ spectra are similar to Ne matrix absorption spectra measured by Maier and coworkers,[19,22,38] except that peaks in the gas-phase spectra are sharper and are displaced slightly to the blue from the Ne matrix peaks. Peak intensities in the REPD spectra depend on the photodissociation efficiency resulting from the 2-colour excitation scheme and are therefore probably less reliable than the relative intensities of peaks in the Ne matrix absorption spectra.

Maier and coworkers assigned most $HC_{2n+1}H^+$ transitions in the visible and UV regions to $\tilde{A}^2\Pi_{u/g} \leftarrow \tilde{X}^2\Pi_{g/u}$, $\tilde{B}^2\Pi_{u/g} \leftarrow \tilde{X}^2\Pi_{g/u}$ and $\tilde{C}^2\Pi_{u/g} \leftarrow \tilde{X}^2\Pi_{g/u}$ band systems, with the latter system carrying the highest oscillator strength.[38] Complications in the spectra of HC_9H^+, $HC_{11}H^+$, $HC_{13}H^+$ and $HC_{15}H^+$ led them to invoke transitions to another electronic state, possibly the $^2\Phi_{g/u}$ state, which may derive intensity through vibronic coupling.[38] The gas-phase spectra are broadly consistent with this previous interpretation, although some of our assignments differ from those in ref. 38, particularly for HC_9H^+, $HC_{11}H^+$ and $HC_{13}H^+$. In our interpretation, the spectra are affected by vibronic interactions, particularly between overtone vibrational levels in the $\tilde{A}$ state manifold and the vibrationless level of the $\tilde{B}$ state. Vibronic mixing of zero-order $\tilde{A}^2\Pi_{u/g}$ and $\tilde{B}^2\Pi_{u/g}$ levels leads to sharing of intensity between the strong $\tilde{B}^2\Pi_{u/g} \leftarrow \tilde{X}^2\Pi_{g/u}$ origin transition and weaker $\tilde{A}^2\Pi_{u/g} \leftarrow \tilde{X}^2\Pi_{g/u}$ overtone transitions. Depending on the size of the chains, the consequence is that instead of the $\tilde{B}^2\Pi_{u/g} \leftarrow \tilde{X}^2\Pi_{g/u}$ origin transition appearing as a single band it is manifested as several peaks. Furthermore, for some chain sizes, higher vibronic levels of the $\tilde{B}^2\Pi_{u/g}$ state are resonant with the lower levels of the $\tilde{C}^2\Pi_{u/g}$ state, further complicating the spectrum. This mixing is particularly evident for $HC_{11}H^+$ for which the interacting zero-order levels are nearly resonant. The nature of the vibronic coupling between the A, B and C states is not clear at this stage, but, given that all three electronic states share the same symmetry, the coupling is probably mediated by totally symmetric CC or CH stretch vibrational modes.

The lowest energy $\tilde{A}^2\Pi_{g/u} \leftarrow \tilde{X}^2\Pi_{u/g}$ band systems exhibit sharp peaks, whose widths are limited by the bandwidth of the OPO ($\approx$5 cm^{-1}). The $\tilde{A} \leftarrow \tilde{X}$ transitions are predicted to be relatively weak with calculated oscillator strengths of 0.0005, 0.0002, 0.0012, 0.0009, and 0.0019 for HC_5H^+, HC_7H^+, HC_9H^+, $HC_{11}H^+$ and $HC_{13}H^+$, respectively.[39] The band shift induced by the Ne matrix for the $\tilde{A} \leftarrow \tilde{X}$ origin transition is -110 cm^{-1} for HC_5H^+, -71 cm^{-1} for HC_7H^+, -9 cm^{-1} for HC_9H^+, -37 cm^{-1} for $HC_{11}H^+$, and -33 cm^{-1} for $HC_{13}H^+$. The $\tilde{A} \leftarrow \tilde{X}$ band systems of the $HC_{2n+1}H^+$ chains exhibit a progression in the acetylenic C$\equiv$C stretch mode, extending to one or two quanta, with a spacing of $\approx$2000 cm^{-1}. For HC_5H^+, a progression in even quanta of the ν_8 mode (the lowest frequency π_g mode) is also observed. As shown in Fig. 3, the wavelength of the $\tilde{A}^2\Pi_{g/u} \leftarrow \tilde{X}^2\Pi_{u/g}$ origin transition increases linearly with the number of carbon atoms in the chain (by $\approx$94 nm for each additional C_2 subunit), akin to other carbon chain series.[13,14,16,17]

Our assignments for the origins of the $\tilde{B}^2\Pi_{g/u} \leftarrow \tilde{X}^2\Pi_{u/g}$ and $\tilde{C}^2\Pi_{g/u} \leftarrow \tilde{X}^2\Pi_{u/g}$ band systems for HC_5H^+ and HC_7H^+ agree

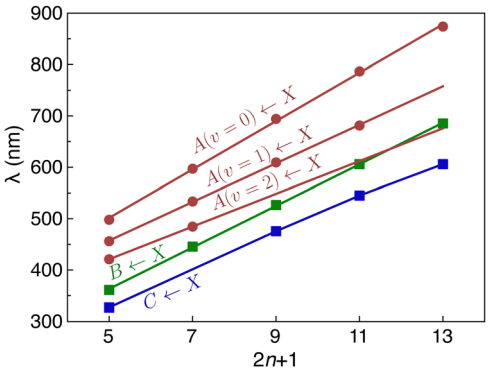

Fig. 3 Wavelengths for the origin transitions of $\tilde{A}^2\Pi_{u/g} \leftarrow \tilde{X}^2\Pi_{g/u}$, $\tilde{B}^2\Pi_{u/g} \leftarrow \tilde{X}^2\Pi_{g/u}$ and $\tilde{C}^2\Pi_{u/g} \leftarrow \tilde{X}^2\Pi_{g/u}$ band systems for $HC_{2n+1}H^+$ chains plotted against the number of carbon atoms ($2n + 1$). Wavelengths for the progression members in the acetylenic C$\equiv$C stretch mode are also plotted for the $\tilde{A}^2\Pi_{u/g} \leftarrow \tilde{X}^2\Pi_{g/u}$ band system. Note that as the chains become longer, overtone vibrational levels (2 quanta of the acetylenic C$\equiv$C stretch mode) associated with the $\tilde{A}^2\Pi_{u/g}$ state come into resonance with the vibrationless level of the $\tilde{B}^2\Pi_{u/g}$ manifold leading to complications in the spectra. The average energy for transitions in the region of the $\tilde{B}^2\Pi_{u/g} \leftarrow \tilde{X}^2\Pi_{g/u}$ origin transition are plotted for HC_9H^+, $HC_{11}H^+$ and $HC_{13}H^+$.

with those of Fulara *et al.*[38] However, for HC_9H^+, $HC_{11}H^+$ and $HC_{13}H^+$, the bands originally assigned to the $\tilde{C}^2\Pi_{g/u} \leftarrow \tilde{X}^2\Pi_{u/g}$ origin transitions are reassigned as origins of the $\tilde{B}^2\Pi_{g/u} \leftarrow \tilde{X}^2\Pi_{u/g}$ band systems, while strong peaks following the linear trend between wavelength and chain length established for the $\tilde{C}^2\Pi_{g/u} \leftarrow \tilde{X}^2\Pi_{u/g}$ origin transitions for HC_5H^+ and HC_7H^+ are assigned as the $\tilde{C}^2\Pi_{g/u} \leftarrow \tilde{X}^2\Pi_{u/g}$ origins for HC_9H^+, $HC_{11}H^+$ and $HC_{13}H^+$. As noted above, it seems that overtones and combinations of vibrational modes associated with the $\tilde{A}^2\Pi_{g/u}$ state interact with the vibrationless level of the $\tilde{B}^2\Pi_{g/u}$ state, leading to mixing and sharing of oscillator strength. These interactions particularly affect the spectrum of $HC_{11}H^+$, and are responsible for a cluster of peaks near 600 nm. Assuming that the zero-order oscillator strength of the $\tilde{B}^2\Pi_{g/u} \leftarrow \tilde{X}^2\Pi_{u/g}$ origin transition greatly exceeds the oscillator strengths for the $\tilde{A}^2\Pi_{g/u} \leftarrow \tilde{X}^2\Pi_{u/g}$ overtone transitions, one can estimate the deperturbed energies for the $\tilde{B}^2\Pi_{g/u}$ state from the centre-of-gravity of the transitions in the origin region (the corresponding wavelengths are plotted in Fig. 3). If this is done, the wavelengths for the deperturbed origin transitions of the three band systems follow linear trends with chain size (see Fig. 3). Significantly, with this new set of assignments there is no need to invoke an additional electronic state to explain the spectra of HC_9H^+, $HC_{11}H^+$ and $HC_{13}H^+$ in the visible region as was done in ref. 38.

A weak band appears approximately 27 cm^{-1} to the red of the $\tilde{A}^2\Pi_{u/g} \leftarrow \tilde{X}^2\Pi_{g/u}$ origin transitions in the HC_5H^+, HC_7H^+, and HC_9H^+ spectra. The two transitions can be assigned to the $^2\Pi_{1/2} \leftarrow {}^2\Pi_{1/2}$ sub-band (strong) and $^2\Pi_{3/2} \leftarrow {}^2\Pi_{3/2}$ sub-band (weak), which are separated by the difference in the spin–orbit splittings for the ground and excited states $\left(\Delta A_{SO} = A''_{SO} - A'_{SO}\right)$. Using the SOC + CASSCF/def2-TZVP method, we calculated spin–orbit splittings for HC_5H^+ $\left(A''_{SO} = 30\ \text{cm}^{-1},\ A'_{SO} = 4\ \text{cm}^{-1}\right)$,

HC_7H^+ $\left(A''_{SO} = 31\ cm^{-1},\ A'_{SO} = 4\ cm^{-1}\right)$, and HC_9H^+ $\left(A''_{SO} = 30\ cm^{-1},\ A'_{SO} = 4\ cm^{-1}\right)$. The calculated ΔA_{SO} values agree with the observed peak separations for HC_5H^+ (26 cm^{-1}), HC_7H^+ (29 cm^{-1}), and HC_9H^+ (27 cm^{-1}). The spin–orbit coupling constants for the $HC_{2n+1}H^+$ ions are similar to those measured for the $\tilde{X}^2\Pi$ and $\tilde{A}^2\Pi$ states of the isoelectronic C_7^- anion $\left(A''_{SO} = 27\ cm^{-1}\right.$ and $\left.A'_{SO} = 0.6\ cm^{-1}\right)$.[56] The relative intensity for the $^2\Pi_{3/2} \leftarrow {}^2\Pi_{3/2}$ sub-band compared to the $^2\Pi_{1/2} \leftarrow {}^2\Pi_{1/2}$ sub-band (10–20%) is consistent with predicted thermal populations of the $^2\Pi_{3/2}$ and $^2\Pi_{1/2}$ levels for molecules in the cryotrap (12% at T = 20 K, assuming a Boltzmann distribution). An alternative assignment of the lower energy peak as a vibrational hot band is less convincing as the vibrational modes should be effectively cooled in the cryotrap. For example, the lowest frequency π_u bend mode (ν_{11}) for HC_5H^+ has a calculated frequency of 128 cm^{-1};[39] at T = 30 K less than 0.4% of the molecules would have a single quantum of ν_{11}.

4.2.1 Formation of $HC_{11}H^+$ from reaction of C_9^+ and C_2H_2. The spectra shown in Fig. 2 clearly show that $C_{2n+1}H_2^+$ chains are generated through the ionization and decomposition of pyrene vapour. From the work of McElvany, it is known that carbon cluster cations react with acetylene to form hydrogenated carbon molecules by the $C_n^+ + C_2H_2 \rightarrow C_{n+2}H_2^+$ association reaction.[43] At low pressure ($\leq 2 \times 10^{-7}$ torr), this reaction occurs at bimolecular collision rates over a size range for which the carbon cluster population exists as mixed linear and cyclic isomers (C_7^+, C_8^+, C_9^+) or only cyclic isomers (C_{10}^+, C_{11}^+, C_{12}^+ C_{13}^+, C_{14}^+).[43] McElvany proposed that the $C_{n+2}H_2^+$ products are formed through radiative association and are essentially $C_n^+ \ldots C_2H_2$ complexes consisting of an acetylene molecules attached to an intact cyclic carbon cluster cation. To explore this hypothesis we investigated $C_{2n+1}H_2^+$ molecules produced by reacting cyclocarbons with acetylene, focussing on $C_{11}H_2^+$ products from the reaction of cyclic C_9^+ and acetylene. To do this, we selected cyclic C_9^+ molecules using the Bradbury–Nielsen ion gate situated at the end of the IMS tube. These mobility-selected C_9^+ ions reacted with acetylene gas introduced into the hexapole ion guide to form $C_{11}H_2^+$ ions, which were subsequently mass-selected by the QMF and introduced into the QIT where they were spectroscopically probed. The scheme is explained in more detail in Section S4 of the ESI.† As shown in Fig. S2 in the ESI,† the $C_{11}H_2^+$ cations formed by reacting C_9^+ with acetylene and $C_{11}H_2^+$ cations generated by exposing pyrene to 266 nm radiation have nearly identical spectra, proving that they share the same linear structure.

To better understand the formation of linear $HC_{11}H^+$ through the bimolecular reaction of C_9^+ and acetylene we constructed a potential energy surface describing the most important reaction steps (Fig. 4). Following the initial encounter, the $C_9^+ + C_2H_2$ reaction proceeds through a series of bicyclic and cyclic intermediates without any prohibitive barrier. The last step involves ring opening to yield the $HC_{11}H^+$ chain, which, in the absence of collisions would have an internal energy above the $\tilde{A}$, $\tilde{B}$ and $\tilde{C}$ excited states. Therefore, it is possible that the nascent $HC_{11}H^+$ product ions are stabilized under low pressure conditions through inverse internal conversion and radiative emission from an excited electronic state (Poincaré fluorescence),[61] or alternatively through emission of infrared radiation. Although we believe that Fig. 4 illustrates a credible mechanism for $C_{11}H_2^+$ chain formation directly from a bimolecular collision, we cannot discount the possibility that a nascent $C_n^+ \ldots C_2H_2$ complex is initially formed by a three body collision in the hexapole, and is collisionally transformed into a linear $C_{11}H_2^+$ chain either in the heaxapole, en route to the QIT, or in the QIT itself. It is also unclear at this stage whether any of the intermediates shown in Fig. 4 are formed in the hexapole and stabilized by collisions with Ar gas ($P \approx 2 \times 10^{-4}$ torr), making their way, along with the linear $C_{11}H_2^+$ chains, into the QIT.

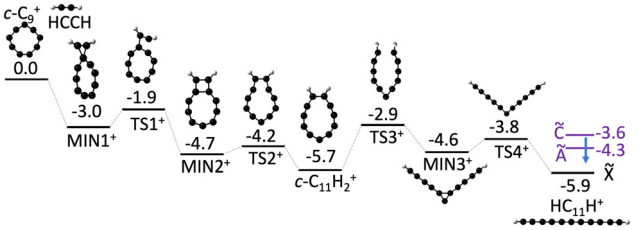

Fig. 4 Proposed formation mechanism for $HC_{11}H^+$ from c-C_9^+ + C_2H_2 reaction. Ground state energies (black bars) are calculated using DFT (ωB97X-D/def2-SVP). Excited state energies (purple bars) for $HC_{11}H^+$ are determined from the spectra shown in Fig. 2. Putative deactivation of $HC_{11}H^+$ product ions by fluorescence from excited electronic states is indicated by a blue arrow. All values are in units of eV.

4.3 Astronomical implications

It is relevant to consider briefly whether any of the $HC_{2n+1}H^+$ chains are DIB carriers. We first consider the relatively narrow $\tilde{A} \leftarrow \tilde{X}$ transitions, which occur in the visible or near infrared regions for $HC_{2n+1}H^+$ (n = 2–6). The stronger $\tilde{B} \leftarrow \tilde{X}$ and $\tilde{C} \leftarrow \tilde{X}$ origin transitions either do not occur in the visible ($C_5H_2^+$), or are broad ($C_7H_2^+$, $C_9H_2^+$, $C_{13}H_2^+$). The exception is the intense $\tilde{C} \leftarrow \tilde{X}$ origin transition of $C_{11}H_2^+$, which we discuss later.

We first consider HC_5H^+, noting that its strongest band in the visible region, the $\tilde{A}^2\Pi_{1/2} \leftarrow \tilde{X}^2\Pi_{1/2}$ origin transition at 498.0 ± 0.2 nm, is reasonably close to DIBs at 497.961 nm and 498.214 nm in spectra for HD 204827.[62] To investigate the possible correspondence between the HC_5H^+ absorption and these nearby DIBs, we recorded the $\tilde{A} \leftarrow \tilde{X}$ origin band at higher resolution using a pulsed dye laser (bandwidth 0.04 cm^{-1}). The spectrum exhibits partial resolution of rotational substructure with an R-branch maximum at 498.02 nm (see Fig. 5). The band was best simulated assuming a temperature of 12 K, a calculated ground state rotational constant B'' = 0.07477 cm^{-1} (computed using CCSD(T)/TZVP), and an excited state rotational constant of B' = 0.07193 cm^{-1} that was adjusted to give the best match between the simulated and measured spectra. It is apparent that the HC_5H^+ band does not correspond to either of the adjacent DIBs and that the match would not improve at higher temperatures. The origin bands for the $\tilde{A} \leftarrow \tilde{X}$ transitions of HC_7H^+, HC_9H^+ and $HC_{11}H^+$, which occur across the visible region, also do not match tabulated DIBs for HD 183143 or HD 204827 sight-lines.[62,63]

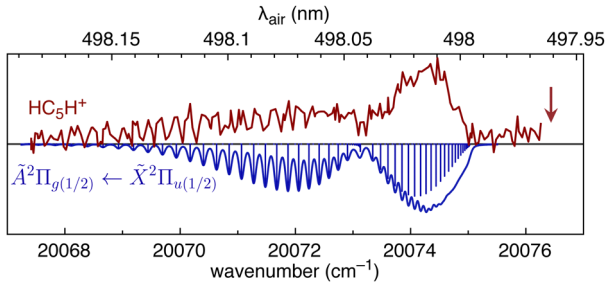

Fig. 5 REPD spectrum of the HC_5H^+ $\tilde{A}^2\Pi_{1/2} \leftarrow \tilde{X}^2\Pi_{1/2}$ band origin measured using a dye laser (bandwidth 0.04 cm^{-1}). The spectrum is compared with a simulation generated using B'' = 0.07477 cm^{-1}, B' = 0.07193 cm^{-1}, and T = 12 K. The vertical arrow indicates the position of the 497.961 nm DIB (data from ref. 62).

The absence of $\tilde{A} \leftarrow \tilde{X}$ origin transitions for HC_5H^+, HC_7H^+, HC_9H^+ and $HC_{11}H^+$ in the HD 183143 or HD 204827 spectra allows one to estimate upper limits for column densities for these sight-lines using the relationship:[64]

$$N = \frac{4\varepsilon_0 m_e c^2}{e^2}\frac{W_\lambda}{\lambda^2 f} \quad (1)$$

where ε_0 is the permittivity of free space, m_e is the electron mass, c is the speed of light, e is the electron charge, λ is the transition wavelength, f is the transition's oscillator strength and W_λ is the equivalent width. Assuming a minimum detectable equivalent width of W_λ = 10 mÅ, implies upper limits for column densities reported in Table 1. Values are given assuming both calculated oscillator strengths (f_{calc}) and experimental oscillator strengths determined from Ne matrix measurements (f_{exp}).[38,39] Unfortunately, there are large differences between the calculated and experimental oscillator strengths, which are reflected in differences in the upper limits for column densities. The upper limits for column densities estimated from the $\tilde{A} \leftarrow \tilde{X}$ transitions are relatively large because the oscillator strengths for these transitions are small.

4.3.1 $HC_{11}H^+$. The strong $\tilde{C}^2\Pi_u \leftarrow \tilde{X}^2\Pi_g$ origin transition of $HC_{11}H^+$ corresponds in position and width to the λ 5450 DIB measured in several astronomical surveys. This can be seen in Fig. 6(a) where the $HC_{11}H^+$ REPD spectrum is plotted together with a synthetic spectrum generated using data for HD 183143.[63] Assuming for the moment that the $\tilde{C}^2\Pi_u \leftarrow \tilde{X}^2\Pi_g$ origin transition is responsible for the λ 5450 DIB, a column density of $\approx 8 \times 10^{12}$ cm^{-2} is estimated using eqn (1) with λ = 5450 Å, W_λ = 0.3595 Å (from ref. 63) and f_{calc} = 0.18 (from ref. 39). A somewhat larger column density of $\approx 5 \times 10^{13}$ cm^{-2} is estimated employing the Ne matrix oscillator strength (f_{matrix} = 0.025).

If $HC_{11}H^+$ is responsible for the λ 5450 DIB, then other weaker $HC_{11}H^+$ bands should also appear in astronomical spectra. The nearby $HC_{11}H^+$ transition at 542.3 nm may contribute to the broad DIB at 542.001 nm (see Fig. 6(a)). Comparisons for other transitions over the 600–700 nm range are difficult because the $HC_{11}H^+$ bands are broad and there is a high density of DIBs in this region. However, the $\tilde{A}^2\Pi_u \leftarrow \tilde{X}^2\Pi_g$ origin transition at 786.8 nm is relatively narrow and occurs in a region where DIBs are sparse, with the nearest DIB at 786.243 nm (see Fig. 6(b)).[63] The $\tilde{A}^2\Pi_u \leftarrow \tilde{X}^2\Pi_g$ transition is estimated to be weaker than the $\tilde{C}^2\Pi_u \leftarrow \tilde{X}^2\Pi_g$ transition by a factor of five based on the matrix oscillator strengths,[38] or by a factor of 200 based on the calculated oscillator strengths.[39] If the matrix oscillator strengths are correct, then the $\tilde{A}^2\Pi_u \leftarrow \tilde{X}^2\Pi_g$ origin transition would have an equivalent width of W_λ = 70 mÅ, making it 4–5 times more intense than the λ 7862 DIB in the HD 183143 spectrum reported in ref. 63 (W_λ = 16 mÅ). In this case the transition should certainly be apparent in existing astronomical spectra. However, if the calculated oscillator strengths are correct, then the $\tilde{A}^2\Pi_u \leftarrow \tilde{X}^2\Pi_g$ origin transition would have an equivalent width of W_λ = 2 mÅ, probably making it difficult to detect.

If $HC_{11}H^+$ exists in the ISM one might expect similar or greater abundances of HC_5H^+, HC_7H^+ and HC_9H^+, although the relative amounts may depend sensitively on their formation mechanisms and the stability of their precursors. If the Ne matrix oscillator strengths are correct, then their column

Table 1 Upper limits for column densities (N_{max}) for $HC_{2n+1}H^+$ chains in diffuse interstellar clouds derived by considering their $\tilde{A} \leftarrow \tilde{X}$ transitions in the visible region and astronomical data for HD 183143.[63] N_{max} values are based on a 10 mÅ minimum detectable equivalent width (W_λ), and use calculated (f_{calc}) and experimental (f_{exp}) oscillator strengths from ref. 39 and ref. 38, respectively. Band positions and widths are taken from the current work. N_{max} values based on f_{calc} are given first and those based on f_{exp} are given second in parentheses

Species	λ nm	f_{calc} (f_{exp})	N_{max} 10^{12} cm^{-2}
HC_5H^+	498.0	0.00046 (0.00075)	100(60)
HC_7H^+	597.1	0.00022 (0.0018)	140(18)
HC_9H^+	694.3	0.00118 (0.004)	20(6)
$HC_{11}H^+$	786.8	0.00089 (0.0046)	20(4)

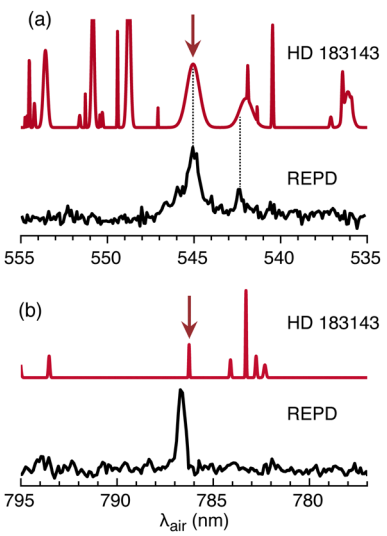

Fig. 6 REPD spectra for $HC_{11}H^+$ in the visible/NIR range for: (a) $\tilde{C}^2\Pi_u \leftarrow \tilde{X}^2\Pi_g$ origin transition; (b) $\tilde{A}^2\Pi_u \leftarrow \tilde{X}^2\Pi_g$ origin transition. In each case, a synthetic astronomical DIB spectrum for HD 183143 generated using data from ref. 63 is shown above the REPD spectrum. Arrows indicate DIBs close to $HC_{11}H^+$ absorptions.

densities should probably exceed 5×10^{13} cm^{-2}, which, according to the upper limits reported in Table 1, would imply that the $\tilde{A}^2\Pi_u \leftarrow \tilde{X}^2\Pi_g$ origin transitions of HC_7H^+, HC_9H^+ and perhaps HC_5H^+ should be apparent in existing astronomical spectra. On the other hand, if the calculated oscillator strengths are correct, the column densities would exceed 8×10^{12} cm^{-2} and the $\tilde{A}^2\Pi_u \leftarrow \tilde{X}^2\Pi_g$ origin transitions of HC_5H^+, HC_7H^+, HC_9H^+ may be too weak to detect.

On balance, the correspondence between the $\tilde{C} \leftarrow \tilde{X}$ origin transition of $HC_{11}H^+$ and the λ 5450 DIB should probably be viewed as a coincidence. Confirmation would require the discovery of other weaker $HC_{11}H^+$ bands in astronomical spectra. As well, one might also expect to observe visible bands for the smaller HC_5H^+, HC_7H^+ and HC_9H^+ species, which would presumably be formed by similar chemical pathways to $HC_{11}H^+$.

5 Conclusions

Electronic spectra of HC_5H^+, HC_7H^+, HC_9H^+, $HC_{11}H^+$, and $HC_{13}H^+$ have been measured in a cryogenically cooled ion trap. The spectra exhibit sharp bands over the NIR, visible and UV ranges, associated with the $\tilde{A}^2\Pi_{u/g} \leftarrow \tilde{X}^2\Pi_{g/u}$, $\tilde{B}^2\Pi_{u/g} \leftarrow \tilde{X}^2\Pi_{g/u}$ and $\tilde{C}^2\Pi_{u/g} \leftarrow \tilde{X}^2\Pi_{g/u}$ band systems. Regular red-shifts of 70–94 nm in wavelength for the origin transitions of these band systems accompanying addition of each C=C unit are disrupted and obscured by vibronic resonances, particularly for the $\tilde{B}^2\Pi_{u/g} \leftarrow \tilde{X}^2\Pi_{g/u}$ transitions of HC_9H^+, $HC_{11}H^+$, and $HC_{13}H^+$.

We find no correspondences between catalogued DIBs and the electronic absorption bands of HC_5H^+, HC_7H^+, HC_9H^+ and $HC_{13}H^+$. However, the strongest $HC_{11}H^+$ band matches the broad λ 5450 DIB. There are two points counting against $HC_{11}H^+$ being a carrier for the λ 5450 DIB. First, less intense bands in the 600–900 nm range in the $HC_{11}H^+$ REPD spectrum are absent from astronomical spectra, although this may be because these bands are much weaker than the 545.1 nm band. Second, there is no evidence in the astronomical spectra for the visible bands of HC_5H^+, HC_7H^+, HC_9H^+ which would presumably have similar or greater abundances than $HC_{11}H^+$. The most promising $HC_{11}H^+$ band for future astronomical detection is probably the $A \leftarrow X$ origin transition at 786.8 nm, which, if $HC_{11}H^+$ is the carrier, should be detectable for sight lines that give a strong signal for the λ 5450 DIB. Better estimates for upper limits of the column densities for HC_5H^+, HC_7H^+, HC_9H^+ and $HC_{11}H^+$ require reliable oscillator strengths for the electronic transitions. Hopefully, fresh experiments or calculations will help resolve the discrepancies between computed and measured oscillator strengths.

The $HC_{2n+1}H^+$ chains may also be detectable in the ISM through their infrared transitions, particularly given the recent advances in IR astronomy with the James Webb Space Telescope. The requisite laboratory infrared spectra should be obtainable using various mass-selective action spectroscopy techniques, including He droplet ion spectroscopy,[65–67] rare gas tagging,[67] or leak-out spectroscopy.[68]

The current study demonstrates that laser ionization/fragmentation of PAHs is an effective strategy for forming highly unsaturated carbon chains. Although $C_{13}H_2^+$ is the largest chain generated from pyrene, even longer species will presumably be produced by ionizing and dissociating larger PAHs. Ultimately, it will be interesting to see whether there is a progressive transition from linear to monocyclic $C_{2n+1}H_2^+$ structures with increasing size, as occurs for $C_{2n+1}H^+$ ions, for which cyclic isomers dominate for species larger than $C_{15}H^+$.[28] Ion mobility measurements for hydrogenated carbon ions generated through laser ablation of graphite in a He/H_2 supersonic expansion suggest that linear and monocyclic isomers are present in roughly equal proportions for $C_{15}H_2^+$ and $C_{17}H_2^+$, and that the monocyclic isomer dominates for $C_{19}H_2^+$ and $C_{21}H_2^+$.[69] Another avenue for future research involves spectroscopically characterizing carbon chains terminated with O or N atoms that are generated using appropriate heterocyclic or substituted PAHs as precursors.

Finally, we note that the strategy of reacting isomer-selected carbon cluster cations with other neutral molecules in the hexapole ion guide has promise for generating exotic molecular ions that can be spectroscopically probed in the cryo-QIT. In the current work the viability of this approach was demonstrated by producing $HC_{2n+1}H^+$ chains as products of the reaction between cyclic carbon cluster cations and acetylene molecules. Although, cyclocarbon cations are relatively stable and do not react with most molecules, the smaller linear carbon chains react with a range of molecules, including H_2, D_2,[44] O_2,[44] CH_4,[44] N_2O,[45] and HCN.[46] It should be relatively straightforward to investigate product ions from these reactions, some of which have astrophysical relevance, using electronic spectroscopy.

Conflicts of interest

There are no conflicts to declare.

Acknowledgements

This research was supported under the Australian Research Council's Discovery Project funding scheme (Project Numbers DP150101427 and DP160100474). The authors thank Richard Mathys from the Science Faculty Workshop for his contributions to the design and construction of the apparatus used in this study.

Notes and references

1 J. Pety, P. Gratier, V. Guzmán, E. Roueff, M. Gerin, J. R. Goicoechea, S. Bardeau, A. Sievers, F. Le Petit, J. Le Bourlot, A. Belloche and D. Talbi, *Astron. Astrophys.*, 2012, **548**, A68.
2 S. Brünken, L. Kluge, A. Stoffels, O. Asvany and S. Schlemmer, *Astrophys. J., Lett.*, 2014, **783**, L4.
3 J. Cernicharo, M. Agúndez, C. Cabezas, R. Fuentetaja, B. Tercero, N. Marcelino, Y. Endo, J. Pardo and P. de Vicente, *Astron. Astrophys.*, 2022, **657**, L16.

4 J. Cernicharo, A. M. Heras, A. Tielens, J. R. Pardo, F. Herpin, M. Guélin and L. Waters, *Astrophys. J.*, 2001, **546**, L123.
5 M. McCarthy, C. Gottlieb, H. Gupta and P. Thaddeus, *Astrophys. J.*, 2006, **652**, L141–L144.
6 K. Taniguchi, P. Gorai and J. C. Tan, *arXiv*, 2023, preprint, arXiv:2303.15769 [astro-ph.GA], DOI: 10.48550/arXiv.2303.15769.
7 A. E. Douglas, *Nature*, 1977, **269**, 130–132.
8 J. P. Maier, G. A. Walker and D. A. Bohlender, *Astrophys. J.*, 2004, **602**, 286.
9 *The Diffuse Interstellar Bands*, ed. A. G. G. M. Tielens and T. P. Snow, Kluwer, Dordrecht, 1995.
10 E. K. Campbell, M. Holz, D. Gerlich and J. P. Maier, *Nature*, 2015, **523**, 322–323.
11 H. Linnartz, J. Cami, M. Cordiner, N. Cox, P. Ehrenfreund, B. Foing, M. Gatchell and P. Scheier, *J. Mol. Spectrosc.*, 2020, **367**, 111243.
12 A. Van Orden and R. J. Saykally, *Chem. Rev.*, 1998, **98**, 2313–2357.
13 E. B. Jochnowitz and J. P. Maier, *Proc. Int. Astron. Union*, 2008, **4**, 395–402.
14 R. Nagarajan and J. P. Maier, *Int. Rev. Phys. Chem.*, 2010, **29**, 521–554.
15 M. A. Duncan, *J. Phys. Chem. A*, 2012, **116**, 11477–11491.
16 C. Rice and J. Maier, *J. Phys. Chem. A*, 2013, **117**, 5559–5566.
17 L. N. Zack and J. P. Maier, *Chem. Soc. Rev.*, 2014, **43**, 4602–4614.
18 P. Freivogel, J. Fulara, D. Lessen, D. Forney and J. P. Maier, *Chem. Phys.*, 1994, **189**, 335–341.
19 J. Fulara, P. Freivogel, D. Forney and J. P. Maier, *J. Chem. Phys.*, 1995, **103**, 8805–8810.
20 D. Forney, P. Freivogel, M. Grutter and J. P. Maier, *J. Chem. Phys.*, 1996, **104**, 4954–4960.
21 X. Chen, M. Steglich, V. Gupta, C. A. Rice and J. P. Maier, *Phys. Chem. Chem. Phys.*, 2014, **16**, 1161–1165.
22 P. Freivogel, J. Fulara, D. Lessen, D. Forney and J. P. Maier, *Chem. Phys.*, 1994, **189**, 335–341.
23 E. K. Campbell and P. W. Dunk, *Rev. Sci. Instrum.*, 2019, **90**, 1–7.
24 J. E. Colley, D. S. Orr and M. A. Duncan, *J. Chem. Phys.*, 2022, **157**, 121102.
25 D. W. Arnold, S. E. Bradforth, T. N. Kitsopoulos and D. M. Neumark, *J. Chem. Phys.*, 1991, **95**, 8753–8764.
26 P. Freivogel, J. Fulara, M. Jakobi, D. Forney and J. P. Maier, *J. Chem. Phys.*, 1995, **103**, 54–59.
27 D. A. Kirkwood, M. Tulej, M. V. Pachkov, M. Schnaiter, F. Güthe, M. Grutter, M. Wyss, J. P. Maier and G. Fischer, *J. Chem. Phys.*, 1999, **111**, 9280–9286.
28 S. J. Marlton, J. T. Buntine, C. Liu, P. Watkins, U. Jacovella, E. Carrascosa, J. N. Bull and E. J. Bieske, *J. Phys. Chem. A*, 2022, **126**, 6678–6685.
29 H. Linnartz, T. Motylewski and J. P. Maier, *J. Chem. Phys.*, 1998, **109**, 3819–3823.
30 T. R. Taylor, C. Xu and D. M. Neumark, *J. Chem. Phys.*, 1998, **108**, 10018–10026.
31 E. Garand, T. I. Yacovitch, J. Zhou, S. M. Sheehan and D. M. Neumark, *Chem. Sci.*, 2010, **1**, 192–201.
32 J. Fulara, M. Grutter and J. P. Maier, *J. Phys. Chem. A*, 2007, **111**, 11831–11836.
33 A. Dzhonson, E. B. Jochnowitz and J. P. Maier, *J. Phys. Chem. A*, 2007, **111**, 1887–1890.
34 C. D. Ball, M. C. McCarthy and P. Thaddeus, *J. Chem. Phys.*, 2000, **112**, 10149–10155.
35 H. Ding, T. W. Schmidt, T. Pino, A. E. Boguslavskiy, F. Güthe and J. P. Maier, *J. Chem. Phys.*, 2003, **119**, 814–819.
36 J. T. Buntine, M. I. Cotter, U. Jacovella, C. Liu, P. Watkins, E. Carrascosa, J. N. Bull, L. Weston, G. Muller, M. S. Scholz and E. J. Bieske, *J. Chem. Phys.*, 2021, **155**, 214302.
37 S. J. Marlton, J. T. Buntine, P. Watkins, C. Liu, U. Jacovella, E. Carrascosa, J. N. Bull and E. J. Bieske, *J. Phys. Chem. A*, 2023, **127**, 1168–1178.
38 J. Fulara, A. Nagy, I. Garkusha and J. P. Maier, *J. Chem. Phys.*, 2010, **133**, 024304.
39 J. Zhang, X. Guo and Z. Cao, *Int. J. Mass Spectrom.*, 2010, **290**, 113–119.
40 M. Mühlhäuser, J. Haubrich and S. D. Peyerimhoff, *Int. J. Quantum Chem.*, 2004, **100**, 53–58.
41 S. Dheandhanoo, L. Forte, A. Fox and D. K. Bohme, *Can. J. Chem.*, 1986, **64**, 641–648.
42 B. Tabone, G. Bettoni, E. F. van Dishoeck, A. M. Arabhavi, S. Grant, D. Gasman, T. Henning, I. Kamp, M. Güdel and P. O. Lagage, *et al.*, *Nat. Astron.*, 2023, 1–10.
43 S. W. McElvany, *J. Chem. Phys.*, 1988, **89**, 2063–2075.
44 S. W. McElvany, B. I. Dunlap and A. O'Keefe, *J. Chem. Phys.*, 1998, **86**, 715–725.
45 M. S. Resat, J. N. Smolanoff, I. B. Goldman and S. L. Anderson, *J. Chem. Phys.*, 1994, **100**, 8784–8794.
46 D. C. Parent and S. W. McElvany, *J. Am. Chem. Soc.*, 1989, **111**, 2393–2401.
47 B. West, F. Useli-Bacchitta, H. Sabbah, V. Blanchet, A. Bodi, P. M. Mayer and C. Joblin, *J. Phys. Chem. A*, 2014, **118**, 7824–7831.
48 H. R. Hrodmarsson, J. Bouwman, A. G. Tielens and H. Linnartz, *Int. J. Mass Spectrom.*, 2022, **476**, 116834.
49 H. R. Hrodmarsson, J. Bouwman, A. G. Tielens and H. Linnartz, *Int. J. Mass Spectrom.*, 2023, **485**, 116996.
50 J. T. Buntine, E. Carrascosa, J. N. Bull, U. Jacovella, M. I. Cotter, P. Watkins, C. Liu, M. S. Scholz, B. D. Adamson, S. J. P. Marlton and E. J. Bieske, *Rev. Sci. Instrum.*, 2022, **93**, 043201.
51 M. Saitow, U. Becker, C. Riplinger, E. F. Valeev and F. Neese, *J. Chem. Phys.*, 2017, **146**, 164105.
52 S. Grimme, S. Ehrlich and L. Goerigk, *J. Comput. Chem.*, 2011, **32**, 1456–1465.
53 F. Weigend and R. Ahlrichs, *Phys. Chem. Chem. Phys.*, 2005, **7**, 3297–3305.
54 B. O. Roos, P. R. Taylor and P. E. Siegbahn, *Chem. Phys.*, 1980, **48**, 157–173.
55 F. Neese, *Wiley Interdiscip. Rev.: Comput. Mol. Sci.*, 2022, **12**, e1606.
56 N. M. Lakin, M. Pachkov, M. Tulej, J. P. Maier, G. Chambaud and P. Rosmus, *J. Chem. Phys.*, 2000, **113**, 9586–9592.

57 U. Jacovella and F. Merkt, *Phys. Chem. Chem. Phys.*, 2017, **19**, 23524–23531.
58 K. Raghavachari, G. W. Trucks, J. A. Pople and M. Head-Gordon, *Chem. Phys. Lett.*, 1989, **157**, 479–483.
59 A. Schäfer, C. Huber and R. Ahlrichs, *J. Chem. Phys.*, 1994, **100**, 5829–5835.
60 M. Mühlhäuser, J. Haubrich, G. Mpourmpakis, A. Mavrandonakis and G. E. Froudakis, *Internet Electron. J. Mol. Des.*, 2003, **2**, 578–588.
61 A. Léger, P. Boissel and L. d'Hendecourt, *Phys. Rev. Lett.*, 1988, **60**, 921.
62 L. M. Hobbs, D. G. York, T. P. Snow, T. Oka, J. A. Thorburn, M. Bishof, S. D. Friedman, B. J. McCall, B. Rachford and P. Sonnentrucker, *Astrophys. J.*, 2008, **680**, 1256.
63 L. M. Hobbs, D. G. York, J. A. Thorburn, T. P. Snow, M. Bishof, S. D. Friedman, B. J. McCall, T. Oka, B. Rachford, P. Sonnentrucker and D. E. Welty, *Astrophys. J.*, 2009, **705**, 32.
64 T. Motylewski, H. Linnartz, O. Vaizert, J. P. Maier, G. A. Galazutdinov, F. A. Musaev, J. Krełowski, G. A. H. Walker and D. A. Bohlender, *Astrophys. J.*, 2000, **531**, 312–320.
65 C. J. Moon, S. Erukala, A. J. Feinberg, A. Singh, M. Y. Choi and A. F. Vilesov, *J. Chem. Phys.*, 2023, **158**, 224307.
66 S. Erukala, A. Feinberg, A. Singh and A. F. Vilesov, *J. Chem. Phys.*, 2021, **155**, 084306.
67 S. Brünken, F. Lipparini, A. Stoffels, P. Jusko, B. Redlich, J. Gauss and S. Schlemmer, *J. Phys. Chem. A*, 2019, **123**, 8053–8062.
68 P. C. Schmid, O. Asvany, T. Salomon, S. Thorwirth and S. Schlemmer, *J. Phys. Chem. A*, 2022, **126**, 8111–8117.
69 S. Lee, N. Gotts, G. von Helden and M. T. Bowers, *J. Phys. Chem. A*, 1997, **101**, 2096–2102.